Title: Interface Tracking Investigation of Geometric Effects on the Bubbly Flow in PWR Subchannels

Authors: Jun Fang[a], Joseph J. Cambareri[b], Michel Rasquin[c, d], Andre Gouws[b], Ramesh Balakrishnan[a], Kenneth E. Jansen[d], Igor A. Bolotnov[b]

Affiliations:

[a] Argonne Leadership Computing Facility, Argonne National Laboratory, Lemont, IL 60439

[b] Department of Nuclear Engineering, North Carolina State University, Raleigh, NC 27695

[c] Computational Multi-Physics Software Development Department, Cenaero, Gosselies, 6041, Belgium

[d] Ann and H.J. Smead Department of Aerospace Engineering Sciences, University of Colorado Boulder, Boulder, CO 80309

Emails: fangj@anl.gov (J. Fang)

jjcambar@ncsu.edu (J.J. Cambareri)

igor_bolotnov@ncsu.edu (I.A. Bolotnov)

Author proof:

Prof. Igor A. Bolotnov

(518) 542-8939

igor_bolotnov@ncsu.edu

Campus Box 7909

3140 Burlington Engineering Labs

2500 Stinson Drive

Raleigh, NC, USA 27695-7909

Manuscript total number of pages: 36

Table list:

Table I: Overview of important geometric and computational parameters. 13

Table II: Locations of measurement planes. 16

Table III: Group defined based on the distance to the wall. 26

Table IV: Groups defined based on the distance from the inlet patch. 26

Figure list:

Fig. 1. The CAD (computer-aided design) model of a 2x2 subchannel structure in the PWR fuel rod bundle with supporting structures and mixing vanes: (a) the inner view with central rod hidden; (b) the outside view; (c) the isolated view of supporting structures and mixing vanes. 12

Fig. 2. Geometric models used in the numerical investigations (front walls are hidden to show the inner structures); dashed lines indicate the locations of measurement planes (MP). 13

Fig. 3. The turbulent eddies (i.e. the hairpin shape structures) induced in the subchannel geometry..... 14

Fig. 4. Initial bubble distribution in the SSC case where the Q-criterion contour is colored by velocity magnitude and the bubble color indicates the corresponding bubble ID. 15

Fig. 5. Initial bubble distribution in the LSC case where the slices present the instantaneous velocity field and 655 bubbles are resolved and colored by their ID's. 15

Fig. 6. A zoom-in view of the near wall mesh, bulk mesh and mesh of the transition region. 15

Fig. 7. Cross-section plane showing the pressure field and overlapped with the measurement plane consisting of static probes (the red spots are bubble/gas regions). 17

Fig. 8. Instentaneous turbulence field at location MPS1. 19

Fig. 9. Distributions of mean liquid and vapor streamwise velocity at locations MPS1 and MPS2..... 19

Fig. 10. Turbulent kinetic energy profiles, and the 19

Fig. 11. Void fraction profiles at locations MPS1 and MPS2. 21

Fig. 12. A zoom-in view about the bubbles in the wake flows of spacer grid and mixing vanes (the bubble color indicates its ID used in bubble tracking algorithms). 21

Fig. 13. The simulated bubbles rising in the vertical long subchannel (LSC) with the instantaneous velocity shown on the back, top and bottom slices. 22

Fig. 14. Distributions of mean liquid and vapor streamwise velocity at four separate measurement locations in the long subchannel LSC. 23

Fig. 15. Turbulent kinetic energy profiles at four separate measurement locations in the long subchannel LSC. 23

Fig. 16. Void fraction profiles at four separate measurement locations in the long subchannel LSC. 24

Fig. 17. Bubble trajectories in the subchannel SSC viewed from the inflow direction (a) and front side (b). 25

Fig. 18. Bubble population history in each distance to wall group for subchannel LSC. 26

Fig. 19. Average bubble relative velocity for the distance to the wall group. 27

Fig. 20. Average group drag coefficient based on the distance to the wall. 27

Fig. 21. Evolution of the average relative velocity for each distance to the wall group as a function of the distance from the domain inlet. 29

Fig. 22. Evolution of the average drag coefficient for each distance to the wall group throughout the LSC domain. 29

Fig. 23. Distribution of bubble drag coefficient immediately before bubbles enter the spacer grid and mixng vane region. 30

Fig. 24. Distribution of bubble drag coefficient immediately after bubbles exit the spacer grid and mixing vane region. 30

Fig. 25. Bubble deformability evolution for each distance to the wall group over the LSC domain. 31

Interface Tracking Investigation of Geometric Effects on the Bubbly Flow in PWR Subchannels

Jun Fang[a], Joseph J. Cambareri[b], Michel Rasquin[c, d], Andre Gouws[b], Ramesh Balakrishnan[a], Kenneth E. Jansen[d], Igor A. Bolotnov[b]

[a] Argonne Leadership Computing Facility, Argonne National Laboratory, Lemont, IL 60439

[b] Department of Nuclear Engineering, North Carolina State University, Raleigh, NC 27695

[c] Computational Multi-Physics Software Development Department, Cenaero, Gosselies, 6041, Belgium

[d] Ann and H.J. Smead Department of Aerospace Engineering Sciences, University of Colorado Boulder, Boulder, CO 80309

fangj@anl.gov (J. Fang); jjcambar@ncsu.edu (J.J. Cambareri); igor_bolotnov@ncsu.edu (I.A. Bolotnov)

ABSTRACT

Absorbing heat from the fuel rod surface, water as coolant can undergo subcooled boiling within the Pressurized Water Reactor (PWR) fuel rod bundle. Due to the buoyancy effect, the vapor bubbles generated will then rise along and interact with the subchannel geometries. The reliable prediction of bubble behavior is of immense importance to ensure the safe and stable reactor operation. However, given a complex engineering system like nuclear reactor, it is very challenging (if not impossible) to conduct high-resolution measurements to study bubbly flows under reactor operation conditions. The lack of a fundamental two-phase flow database is hindering the development of accurate two-phase flow models required in more advanced reactor designs. In response to this challenge, first-principles based numerical simulations are emerging as an attractive alternative to produce a complementary data source along with experiments. Leveraged by the unprecedented computing power offered by state-of-the-art supercomputers, direct numerical simulation (DNS), coupled with interface tracking methods (ITM) is becoming a practical tool to investigate some of the most challenging engineering flow problems. In the presented research, the turbulent bubbly flow is simulated via DNS in single PWR subchannel geometries with auxiliary structures (e.g. supporting spacer grid and mixing vanes). The geometric effects these structures exert on the bubbly

flow are studied with both conventional time-averaging approach and novel dynamic bubble tracking method. The new insights obtained will help inform better two-phase models that can contribute to safer and more efficient nuclear reactor systems.

KEYWORDS

DNS, Interface Tracking, Bubble Tracking, PWR Subchannel

I. INTRODUCTION

During the normal operation conditions of PWRs, subcooled nucleate boiling can take place when the temperature of bulk flow is slightly lower than the saturation temperature. The generation of vapor bubbles promotes the coolant turbulence intensity, and thus leads to a better convective heat removal performance.[1] However, this efficient heat transfer mechanism is limited by the departure from nucleate boiling (DNB) phenomenon.[2] The critical heat flux is the characteristic parameter beyond which the heat transfer coefficient drops significantly leading to a rapid temperature excursion of the nuclear fuel rods. Overheating of the fuel rods may result in long term structure damage of the reactor core. To guide and inform PWR designs, numerical simulations of reactor systems remain the major practical and cost-efficient approach.[3,4] There are many thermal-hydraulics (TH) codes developed in the nuclear community nowadays, such as RELAP5[5], TRACE[6] and so on. However, most two-phase closures being used in these TH codes are still 1-D or even 0-D models. To better predict the two-phase flow behavior in reactor cores, more accurate and multi-dimensional two-phase turbulence models are desired.

Historically, the modeling of two-phase turbulent flow evolved from the earliest homogeneous mixture[7,8] (1930's and 1940's), mixture models involving slip correlations[9] (1950's and 1960's), and then into two-fluid modeling[10] (1970's to present). In 1992, Lahey and Drew[11] derived a three dimensional two-fluid model of vapor/liquid two-phase flows using ensemble averaging. As stated by the authors, the key to accurate two-fluid modeling is the interfacial and wall closure terms. In nuclear engineering applications, the development and validation of two-phase turbulence models/closures call for reliable and high-fidelity data concerning the reactor geometry and flow conditions. Although experiments remain the primary data source, validated computational approach provides valuable flexibility to represent the reactor core conditions as well as relatively easier access to the crucial flow data of interest.[12] With no turbulence model utilization, DNS has been widely accepted as a reliable numerical data source for the development and validation of turbulence models along with experiments. As the most computationally expensive approach compared to other CFD techniques, DNS applications used to be limited to flow studies at low Reynolds

numbers. Thanks to the tremendous growth of computing power over the past decades, the simulation capability of DNS has now started overlapping with some of the most challenging engineering problems.[13]

Equipped with the interface tracking method, the DNS capability can be extended to simulate the two-phase turbulent flows.[14,15] There are three prominent interface tracking methods: volume of fluid method[16], front tracking method[17] and level set method[18]. Interface tracking methods utilize various schemes to explicitly or implicitly track the location of gas-liquid interfaces.[19] This tracking process generally relies on a marker (i.e. phase indicator) function that can be advected by the flow. The phase indicator function plays a two-fold role: (1) it is used to determine interface location and represent interface topology change; (2) it is used to determine the material properties of different phases, such as density and viscosity. Each method has its own strengths and limitations. The level set method is adopted in the current computations due to some favorable features it retains. For example, level set method can provide accurate interface curvature information, allow bubble coalescence and breakup to occur without user intervention, and also support straight-forward implementation for unstructured grid solvers.[12]

In the presented research, the PWR subchannel geometry is selected as the computational domain considering its important role in reactor thermal-hydraulics analyses. Two subchannel geometries with different heights are studied herein. While rising under the buoyant effect, the simulated bubbles would interact with fuel rod surfaces as well as the auxiliary core structures (e.g. supporting spacer grid and mixing vanes). In the simulations, bubble interfaces can be readily tracked by the level set. However, the traditional level set method cannot associate the calculated flow information with specific bubbles when multiple bubbles are present in the domain. This drawback hinders the collection of valuable bubble parameters, which may offer in-depth insights about bubbly flow behavior. To address this drawback, a bubble tracking method has been recently developed[20–22] and applied in the current work. Both the mean turbulence profiles and advanced bubble tracking results are to be presented to show the geometric effect of subchannel structures on bubble behavior. This new simulation capability will help shed light onto the bubbly flows inside PWR relevant geometries and better assess the influence of spacer grid and mixing vanes on two-phase coolant flows.

II. NUMERICAL METHOD

PHASTA code is being used in current simulations, which is a three-dimensional finite element method (FEM) flow solver for both incompressible and compressible flows. Incorporated with a level set algorithm, PHASTA has been used to simulate various two-phase flows.[23,24] The bubble tracking method is recently developed and implemented in PHASTA to collect detailed bubble parameters.[22] In addition, PHASTA supports unstructured grid, which makes it adequate for simulations of turbulent flows in complex geometries, such as the 2x2 PWR fuel bundle structure with spacer grids and mixing vanes.[25] Together with the highly scalable performance on massively parallel computers[26], PHASTA is a promising tool for advanced modeling of turbulent two-phase flows. The outstanding scalability of PHASTA has already been demonstrated[26], with up to 768×1024 processors on the IBM Blue Gene/Q Mira system operated by Argonne National Laboratory, which is the #17 fastest supercomputer in the world as of June 2018.

II.A. Governing equations

PHASTA version considered in this work solves the Incompressible Navier-Stokes (INS) equations directly in three dimensions using a stabilized finite element method (FEM).[27] The spatial and temporal discretization of the INS equations within PHASTA has been previously discussed in Nagrath et al.[23] The strong form of INS is given by

Continuity:
$$\frac{\partial u_i}{\partial x_i} = 0 \tag{1}$$

Momentum:
$$\rho \frac{\partial u_i}{\partial t} + \rho u_j \frac{\partial u_i}{\partial x_j} = -\frac{\partial p}{\partial x_i} + \frac{\partial \tau_{ij}}{\partial x_j} + f_i \tag{2}$$

where u_i is the velocity in the i-th dimension (i = 1, 2 and 3), ρ denotes the density of the fluid, p the static pressure and τ_{ij} the viscous stress tensor. f_i represents the i-th component of the body force vector. For the

incompressible flow of a Newtonian fluid, the viscous stress tensor is related to the fluid viscosity μ and the strain rate tensor, S_{ij}, as:

$$\tau_{ij} = 2\mu S_{ij} = \mu(\frac{\partial u_i}{\partial x_j} + \frac{\partial u_j}{\partial x_i}) \tag{3}$$

Employing the Continuum Surface Force (CSF) model proposed by Brackbill et al.[28], the surface tension force is modeled as a local volumetric force density across the interface region (included in f_i).

II.B. Level set method

Introduced by Osher and Sethian[29] and further developed by Sussman et al.[18], the level-set method has been widely used as one of the major interface tracking approaches in multiphase flow simulations. PHASTA incorporates this level-set method to extend the simulation capability from single-phase to two-phase flows.[23] The bubble interface is modeled as the zero-level set of a smooth function, φ, where φ is called the first scalar and is represented as the signed distance from the zero-level set. That is, at $\varphi = 0$, the level set defines the interface. The scalar, φ, is advected with the fluid according to the advection Eq. (4). The liquid phase is indicated by a positive level set, $\varphi > 0$, while the gas phase by the negative, $\varphi < 0$.

$$\frac{D\varphi}{Dt} = \frac{\partial \varphi}{\partial t} + \boldsymbol{u} \cdot \nabla \varphi = 0 \tag{4}$$

Evaluating the jump in physical properties across gas-liquid interface using a step change is challenging numerically[30]; instead, a finite interface thickness is assumed[17], and the properties over the interface are determined using a smoothed Heaviside kernel function given by Eq. (5) below. Wherever there are significant gradients in the velocity, the distance field will become distorted. If not corrected, the interface thickness will likewise be distorted, and false interfaces may be created. To maintain an accurate distance field, the level set field is corrected at every time iteration with a re-distancing operation, also known as re-initialization process. A detailed description of the advection and re-distancing processes has been documented before in Nagrath et al.[23] and Bolotnov et al.[24]

$$H_\varepsilon(\varphi) = \begin{cases} 0 & \text{for } \varphi < -\varepsilon \\ \frac{1}{2}\left[1 + \frac{\varphi}{\varepsilon} + \frac{1}{\pi}\sin\left(\frac{\pi\varphi}{\varepsilon}\right)\right] & \text{for } |\varphi| < \varepsilon \\ 1 & \text{for } \quad \varphi > \varepsilon \end{cases} \tag{5}$$

II.C. Bubble tracking method

As mentioned above, the level set ITM utilizes a signed distance field to represent the phases separated by an interface. One can readily distinguish the gas phase from the liquid based on the corresponding level set value. However, little attention has been paid in the past to the distinction and tracking of individual bubbles in the two-phase flow[22]. When it comes to the individual bubble level, the level set method lacks the capability to distinguish a given bubble from other ones. Tracking the bubbles would allow to collect the detailed information regarding the individual bubble behavior, such as bubble velocity, volume, deformation level, and even the local liquid velocity and shear rate. Such type of bubble information is very valuable for the development of better closure laws that can lead to more accurate predictions of turbulent bubbly flow. To track and collect data of bubbles, a bubble indicator field is initialized and can be successfully advected to dynamically track each of the simulated bubbles. Associated data extraction techniques are developed as well to record the important parameters of bubble behavior and local fluid conditions. More details about bubble tracking development and implementation can be found in previous publications.[22,31]

II.D. DNS mesh design

The following requirements must be met to ensure an accurate representation of relevant turbulent scales and bubble behavior in the simulations: (a) the computational domain must be sufficiently large to contain the largest turbulent eddies; (b) the grid spacing must be sufficiently small to resolve the small scales of interest in liquid turbulence; (c) the resolution of bubble interface and the vicinity regions should be fine enough to properly capture the interface topology changes as well as the eddies in the wake flow behind a bubble. The periodic inlet/outlet condition is adopted to allow the proper resolution of the large

turbulent eddies in the flow. To meet the second prerequisite, the mesh cell sizes should be comparable to the local Kolmogorov length scale. Since the calculation of the Kolmogorov scale requires values of the turbulence dissipation rate, which are not known a priori, several scoping runs are first performed to get the approximated Kolmogorov length scales. The computational mesh is refined if the existing mesh cell size is much larger than the Kolmogorov scale. This iterative process is done till an adequate mesh for DNS purpose is obtained. Interested readers are referred to the work of Fick et al.[32] for more details regarding the general DNS mesh design. Last but not least, in the two-phase flow DNS, additional attention must be paid to ensure that the mesh designed is sufficient to capture the interface behavior and the bubble induced turbulence. Earlier meshing studies have indicated that PHASTA code requires at least a resolution of 20 elements across the diameter (EAD) to properly reflect the interface topologic change.[33] To assess the mesh readiness in resolving the bubble induced turbulence, another meshing study was done by Fang and Bolotnov[22] by comparing the turbulence kinetic energy (TKE) increment around the bubble with various bubble resolutions. It was found out that a minimum bubble resolution of 20 EAD is required to capture most of the TKE increment due to the bubble's existence. Considering the balance between efficiency and accuracy, a bubble resolution of 20 EAD is adopted for the current interface tracking investigations.

III. PROBLEM DESCRIPTION

In nuclear reactor cores, the nuclear fuel rods are generally arranged together as rod bundles in a triangular or square lattice. A small portion of a typical PWR fuel rod bundle is illustrated in Fig. 1a, where the intermediate flow mixing (IFM) grids are also represented.[34] The conduit space among the fuel rod bundle can be further divided into subchannels (four subchannels are shown in Fig. 1b). The coolant flow moving through the subchannels will carry the generated heat from the reactor core to stream generators. The mixing vanes installed (Fig. 1c) play a crucial role in enhancing the coolant turbulence intensity, and thus promoting the convective heat removal efficiency from fuel rod surfaces. Under the normal PWR operation conditions, subcooled boiling can take place to produce vapor bubbles in the coolant flow in the upper part of the core. The existence of bubbles usually further increases the heat removal efficiency due

to bubble induced turbulence.[35] However, the bubble behavior in PWR subchannels and its comprehensive impact on reactor operation are yet to be fully understood due to the high-resolution measurement difficulties in the high temperature high pressure radioactive reactor core environment.

Given the available computing resources, two relatively simplified geometries are selected herein as the computation domains to study the geometric effects of spacer grid and mixing vanes on the bubbly flow. The first domain is a short subchannel (SSC) with reduced size spacer grid and two mixing vanes, shown in Fig. 2. In addition to the SSC domain, a longer subchannel (LSC) is also studied where the internal structures are the same as those in SSC. Meanwhile, the LSC domain is carefully designed to preserve the height ratio between the spacer grid and the 'unblocked' subchannel separating two consecutive spacer grids. That ratio is roughly 1:10 in a realistic PWR subchannel design. The selected flow rate results in nearly the same bubble residence time at the spacer grid region in each flow through period as in PWR core normal operating conditions. The dashed lines in Fig. 2 indicate the locations of measurement planes (MP) that were used to record instantaneous flow field information. More geometric details are listed in Table I.

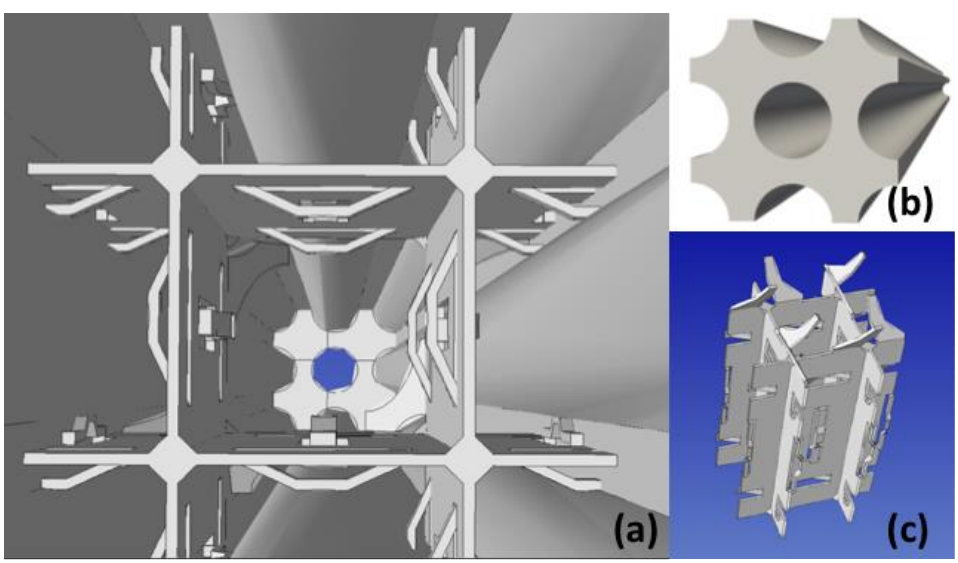

Fig. 1. The CAD (computer-aided design) model of a 2x2 subchannel structure in the PWR fuel rod bundle with supporting structures and mixing vanes: (a) the inner view with central rod hidden; (b) the outside view; (c) the isolated view of supporting structures and mixing vanes.

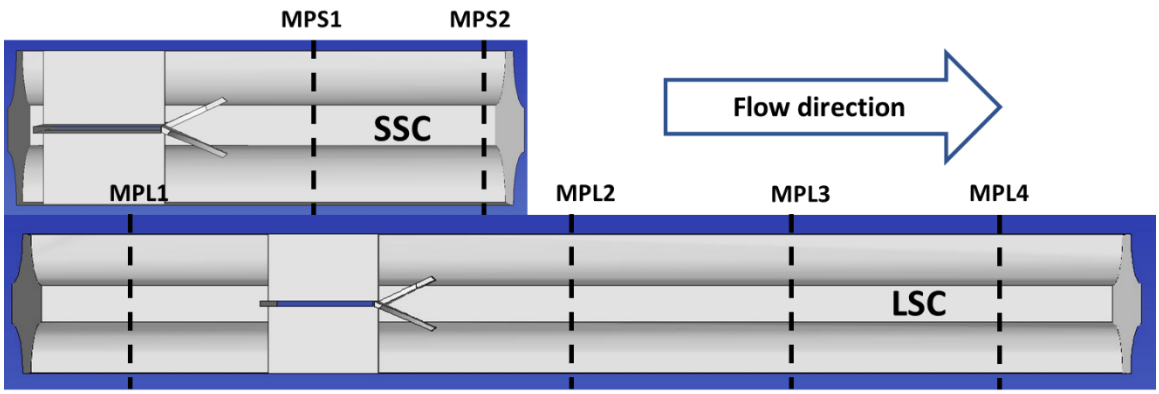

Fig. 2. Geometric models used in the numerical investigations (front walls are hidden to show the inner structures); dashed lines indicate the locations of measurement planes (MP).

Table I: Overview of important geometric and computational parameters.

Geometry/Case	**SSC**	**LSC**
Rod radius (*mm*)	4.57	
Aspect ratio[1]	1.38	
Domain height (*mm*)	40.5	100.0
Vertical coordinate range (*mm*)	0 to 40.5	-20.0 to 80.0
Spacer grid height (*mm*)	10.0	10.0
Mixing vane height (*mm*)	5.0	5.0
Height ratio between spacer grid and the subchannel section	1:4	1:10
Mesh cell size in bulk region (μm)	29.30	
Mesh cell size of the first boundary layer mesh (μm)	8.14	
Total number of mesh cells	1.10 B	2.50 B
Time step size (*s*)	1.0×10^{-5}	1.0×10^{-5}
Number of time steps computed	3450	3850
Number of time steps for one flow through	5400	13500
Number of flow through obtained	0.64	0.28
Computational cost for one flow through (*CPU-hour*)[2]	5.51 M	47.13 M
Number of bubbles resolved	262	655

For both domains, periodic boundary conditions are applied to the domain inlet/outlet as well as transverse faces. No-slip wall conditions are applied to both the fuel rod surface and the surfaces of the spacer grid and mixing vanes. The gravitational force is in the opposite direction of the mean flow to represent an upflow condition. Single-phase turbulence is first generated prior to introducing bubbles in the computational domain. Thanks to the presence of spacer grid and mixing vanes, single-phase turbulence field is efficiently created in the domains, and the eddies around spacer grid and mixing vanes are shown

[1] The aspect ratio is the ratio of the distance between two fuel rod centers over the rod diameter.

[2] The Computational cost is estimated on the BG/Q Mira HPC at Argonne National Laboratory.

in Fig. 3. Through the adjustment of the flow-driving pressure gradient in the streamwise direction, the coolant flow can achieve the desired turbulence profiles. A dedicated bubble initialization code is developed and utilized to produce the initial bubble positions, radii and associated bubble ID's. Based on the single-phase turbulence solution and bubble information provided, PHASTA can initialize the level set distance field and bubble ID field for subsequent two-phase flow simulations (as shown in Fig. 4 and Fig. 5). A 1% void fraction is considered in both cases, which results in 262 and 655 bubbles resolved respectively, and all the bubbles have a uniform diameter of 0.65 *mm* (an initially spherical shape).

The mean flow velocity is 0.75 *m/s* in both cases, which corresponds to a Reynolds number (Re_h) of roughly 80,000 based on the subchannel hydraulic diameter. The discretization results in 1.10 B and 2.50 B mesh cells/elements for the domain SSC and LSC, respectively. The bulk region (away from the walls) consists of isotropic mesh elements whose size is equivalent of the Δy^+ of 9.0, where $\Delta y^+ = u_\tau \Delta y/\nu$, $u_\tau = \sqrt{\tau_w/\rho}$, where τ_w is the wall shear stress. A refined mesh is specified in the near wall regions, and the thickness of boundary layer mesh cells ranges from Δy^+ of 2.5 to 9.0 (shown in Fig. 6). The computational meshes are partitioned with the Chef utilities developed at SCOREC to up to 512K parts on Mira for efficient parallel runs.[36] The viscosities and densities of the liquid/gas phases are determined by using the saturated properties of water and vapor at 300 °*C*.[37]

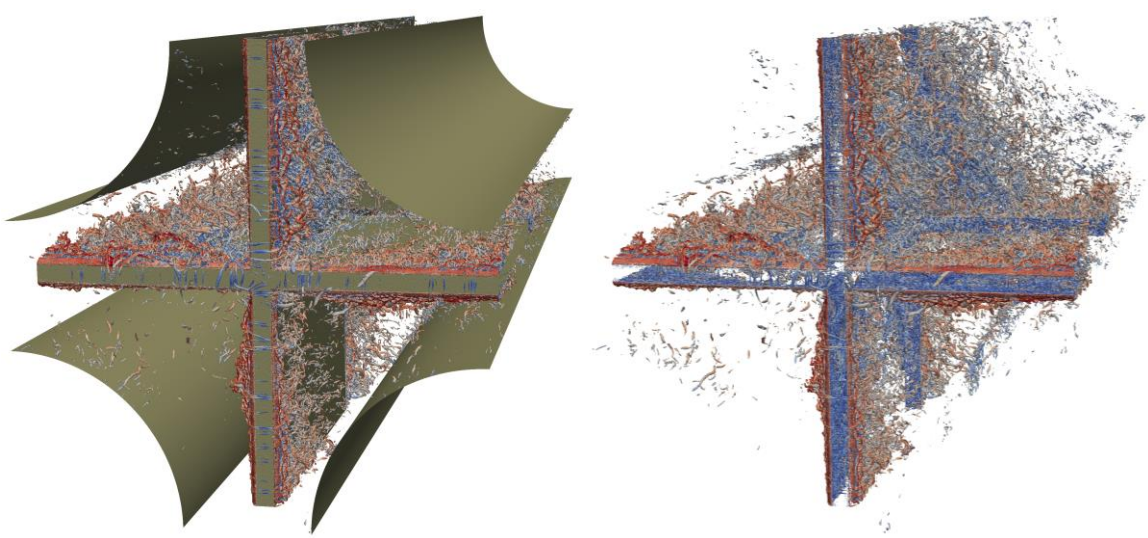

Fig. 3. The turbulent eddies (i.e. the hairpin shape structures) induced in the subchannel geometry.

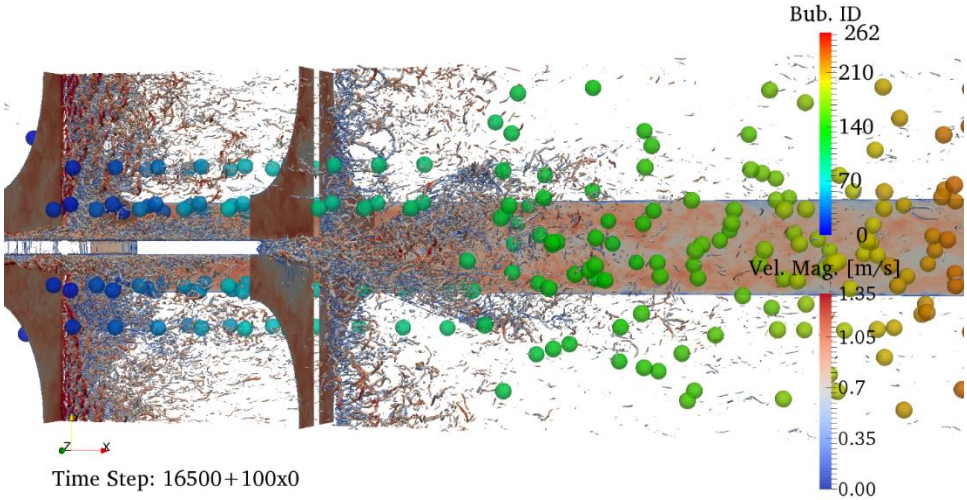

Fig. 4. Initial bubble distribution in the SSC case where the Q-criterion contour is colored by velocity magnitude and the bubble color indicates the corresponding bubble ID.

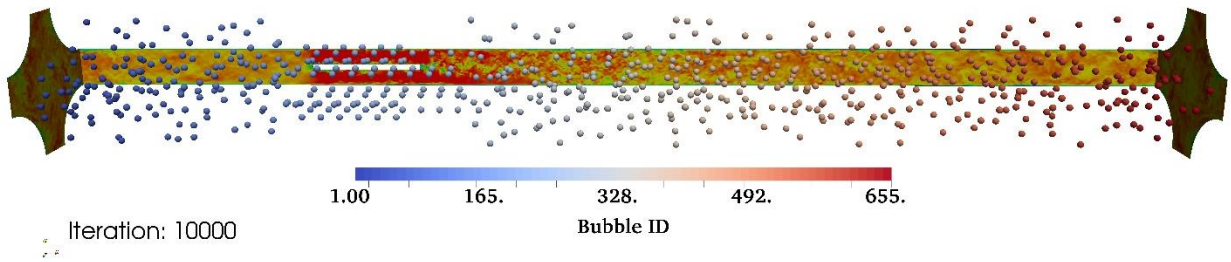

Fig. 5. Initial bubble distribution in the LSC case where the slices present the instantaneous velocity field and 655 bubbles are resolved and colored by their ID's.

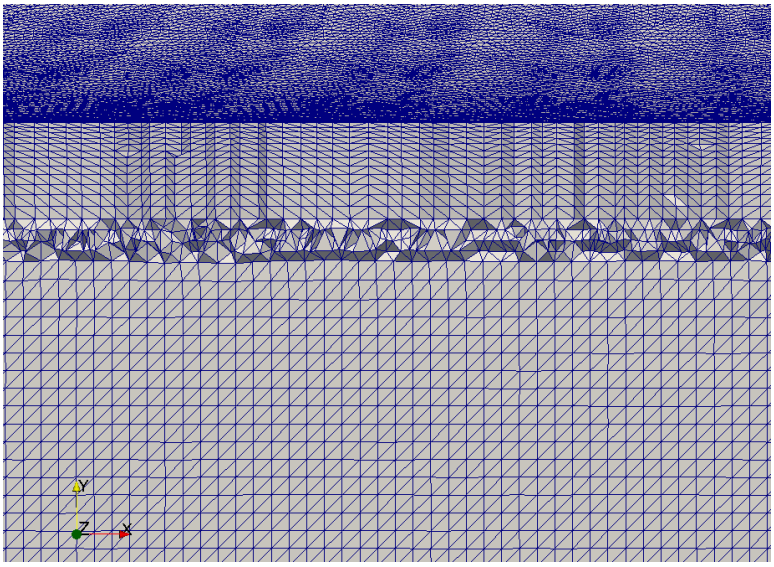

Fig. 6. A zoom-in view of the near wall mesh, bulk mesh and mesh of the transition region.

As shown in Fig. 7, our conventional averaging analysis of turbulent flows relies on a series of virtual probes placed in the domain. These probes can be used to collect the instantaneous flow field information. The post-processing of the recorded turbulence data can produce various time-averaged turbulence quantities[37], such as the mean flow velocity, turbulent kinetic energy and void fraction distribution profile for two-phase cases. As listed in Table II, two probe planes/MPs are placed in the domain SSC, while four MPs are used in the domain LSC to better assess the influence of mixing vanes at different downstream locations. Averaging procedures always involve a certain loss of information. Consequently, the conventional approach is found not very adequate for the study of dynamic transient problems of bubbly flow. Specifically, the conventional averaging approach cannot capture precisely the interaction between the bubbles with geometrical constraints and the resulting instantaneous thermal-hydraulic response. To the contrary, the advanced analysis supported by bubble tracking takes a different approach.[22] Through the bubble tracking method, one can access the full history regarding the behavior of all simulated bubbles, such as bubble trajectories, evolution of bubble shape, velocity and so forth. The next step is to apply statistical analysis methods and to find out the correlations between certain bubble behavior with bubble and local liquid conditions. The present study examines the drag force, bubble migration and bubble deformation patterns in PWR subchannels and how these bubble dynamics are influenced by the geometric structure in PWR subchannels.

Table II: Locations of measurement planes.

Geometric model	**Measurement plane**	**Distance from the mixing vanes endpoint (*mm*)**
SSC	MPS1	7.83
	MPS2	20.83
LSC	MPL1	72.83
	MPL2	12.83
	MPL3	32.83
	MPL4	52.83

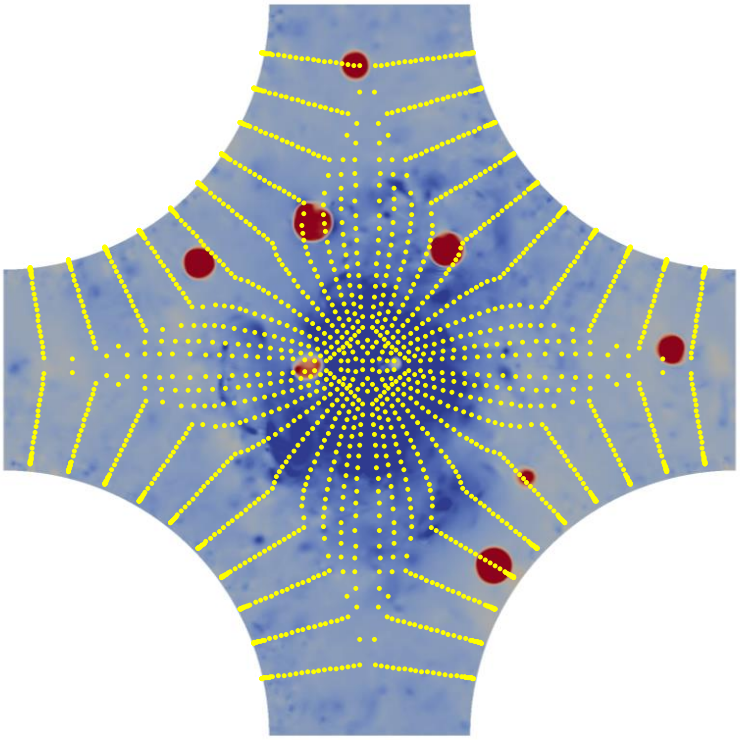

Fig. 7. Cross-section plane showing the pressure field and overlapped with the measurement plane consisting of static probes (the red spots are bubble/gas regions).

IV. RESULTS AND DISCUSSION

Both single- and two-phase flow simulations are carried out on IBM Blue Gene/Q MIRA platform at Argonne National Laboratory (ANL). Compared to the single-phase simulations, the two-phase cases are generally more expensive to run. Besides the level set advection, the re-distancing and bubble tracking algorithms also impose additional computational costs. Moreover, stringent CFL constraints must be satisfied to ensure the numerical stability and bubble shape and motion-time resolution in two-phase computations. However, these overheads are justified by the insightful bubble data extracted from two-phase turbulent flows. Shown in Fig. 4 and Fig. 5, the resolved bubbles are expected to interact with auxiliary structures and the interaction is discussed in the next paragraphs. The single-phase turbulence statistics has been presented in previous papers[13,37]. This paper will primarily focus on the two-phase flow analysis with both conventional time averaging techniques and the novel advanced analysis based on dynamic bubble tracking method. Due to the high computational costs (Table I), the bubbly flow case of

LSC (which has 2.5 B mesh cells in the domain) is still on the early stage of mixing. Despite that a fully steady state has not been reached for all statistics yet, preliminary conclusions can already be drawn. More importantly, the numerical tools developed in this framework can be readily used in future analysis when more simulation results are available. As for the sample size of time averaging analysis, the two-phase flow data base covers a range of about 30 bubble diameter time in both cases. One bubble diameter time here is defined as the average time interval during which a bubble migrates one diameter distance. The time averaging turbulence analysis processes the instantaneous turbulent flow field information to obtain the mean streamwise velocity, turbulence kinetic energy and the void fraction profile at different locations with respect to the fuel rod surface. The averaging is done for a specific time interval and along all probes which have the same wall distance. In addition, bubble tracking analysis can process the detailed bubble information recorded from its entire lifetime over the course of bubbly flow simulations. This novel approach will help reveal in-depth insights, including the bubble drag force distribution and other bubble behavior patterns that depend on geometric constraints and local flow conditions.

Two downstream static probe planes are used in the two-phase flow simulations in domain SSC (as listed in Table II). Due to the existence of internal structures in the subchannel, especially the mixing vanes, a strong centrifugal effect is identified in the flow as observed in Fig. 8. The mixing vanes forcefully push the liquid flow towards the periphery regions (closer to the walls or fuel rod surface) and create a rotating swirl downstream the mixing vanes. As a result, the mean streamwise velocity of both liquid and vapor phases is reduced towards the center of the channel as shown in Fig. 9. This differs significantly from the mean velocity profiles observed in subchannel geometries where these spacer grid and mixing vanes are not present.[37] Without spacer grid and mixing vanes, the mean velocity profile would be flattened outside the boundary layer region all the way to the domain center. Besides the mean velocity profile, the impact of auxiliary structures on turbulent kinetic energy (TKE) is also prominent. As shown in Fig. 10, a strong TKE peak is observed at the wall distance of 2.89 *mm* (or 1.45 *mm* from the domain centerline). Considering the size of mixing vanes, the relative position of TKE peak from the domain centerline is 2/3 of that of the mixing vane tip (Fig. 10).

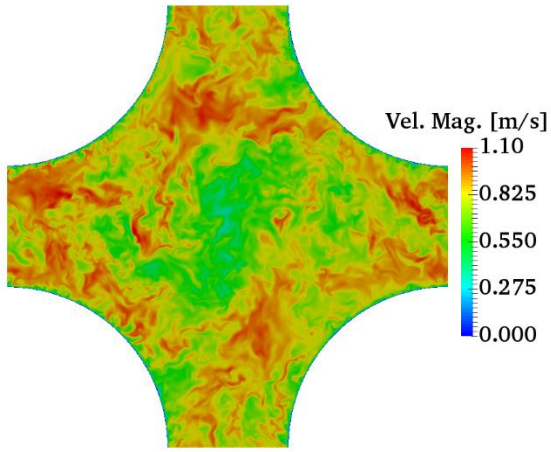

Fig. 8. Instentaneous turbulence field at location MPS1.

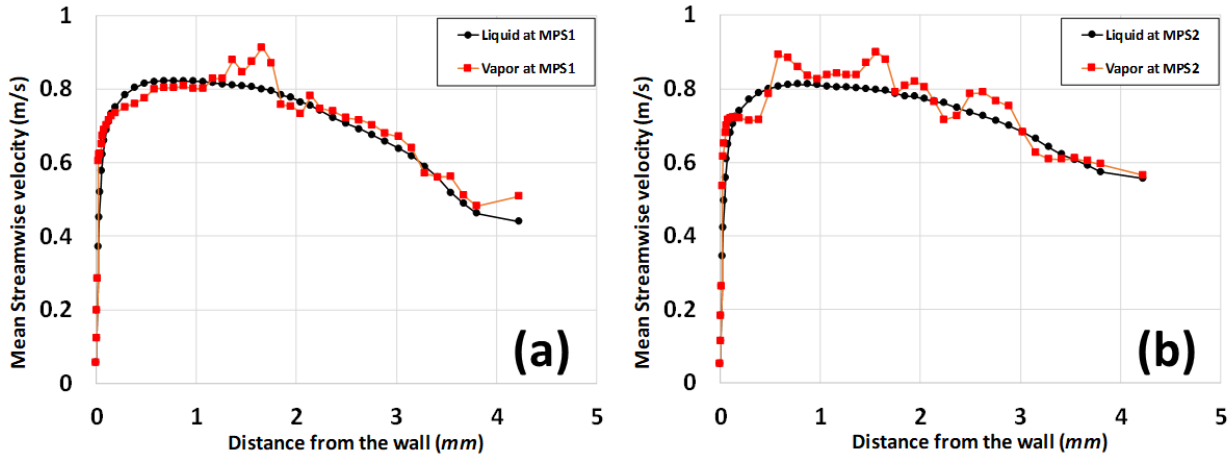

Fig. 9. Distributions of mean liquid and vapor streamwise velocity at locations MPS1 and MPS2.

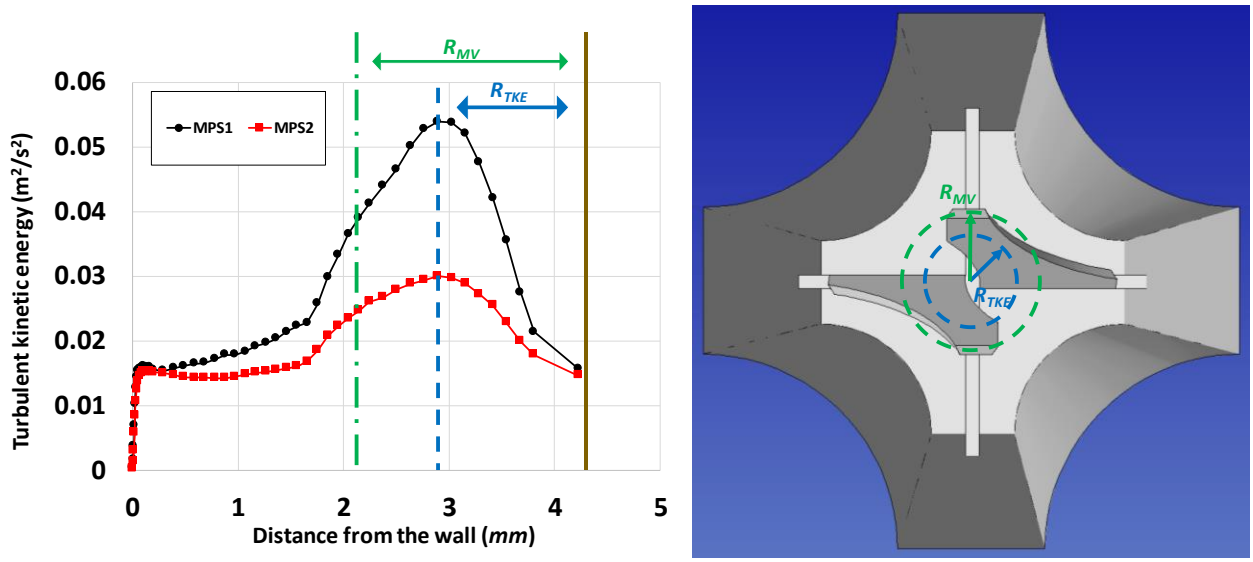

Fig. 10. Turbulent kinetic energy profiles, and the relative position of the TKE peak (R_{TKE}) versus that of the mixing vane tip (R_{MV}).

The existence of the spacer grid and mixing vanes also substantially alters the distribution of void fraction (or vapor volume fraction) in the subchannel (Fig. 11). Note that the two-phase flow typically displays a wall peaked void fraction profile for an empty subchannel (i.e. no internal structure/geometric constraints). To the contrary, a center peak is observed here at both probe measurement planes instead of the wall peak. This phenomenon is directly related to the centrifugal effect imposed by the mixing vanes. Because the liquid is pushed to the periphery regions, bubbles are driven simultaneously towards the opposite direction, that is the domain center, due to the relatively low density/weak inertia compared to ambient liquid. A close view about the bubbles in the wake flows of spacer grid and mixing vanes is presented in Fig. 12. Regarding the relative positions, MPS2 is at the further downstream location and its peak height is slightly lower than that of MPS1.

In the longer channel of domain LSC, four probe measurement planes are employed in the related bubbly flow simulations. This allows the comparison of the geometric effects of spacer grid and mixing at various downstream locations in a meaningful way. A series of solution screenshots in Fig. 13 shows the bubble migration along with the upflow through the long subchannel geometry. The profiles of time averaged liquid and vapor velocity are plotted in Fig. 14. The wall is represented by a wall distance of zero and the domain center is located at the distance of 4.34 *mm*. Like Fig. 9, the mean velocity profiles at the domain center are all bended down at different levels. According to the relative distance from the mixing vanes (as listed in Table II), the sequence of measurement planes is MPL2, MPL3, MPL4 and then MPL1. Together with the profiles shown in Fig. 14, it is obvious that the influence of spacer grid and mixing vanes decays as the downstream flow move further away from the mixing vanes. The profile at MPL2 exhibits the highest level of bending while the profile at MPL1 is the closest to a flattened distribution. The same decay pattern is also captured on the profiles of TKE at separate downstream locations shown in Fig. 15. Although the peak heights of TKE profile are different, the peak location is very consistent ranging from 2.63 *mm* to 2.89 *mm* with very minor difference. The same peak location is also observed in the shorter subchannel SSC which is visually illustrated in Fig. 10. As for the void fraction profiles (shown in Fig. 16),

no significant difference is observed with the time averaging analysis techniques except the peak height at MPL3 is lower than the rest. Unlike other turbulence quantities such as mean velocity or TKE, the calculation of void fraction profile requires more statistics to be collected as gas only accounts for 1% volume in the domain. Given the relatively small sample size, it is difficult to draw meaningful conclusions with void fraction profiles here. In the following discussions, In the following discussions, the bubble tracking analysis demonstrates its potential and provides a new perspective to study and understand the bubble behavior in the subchannel geometries.

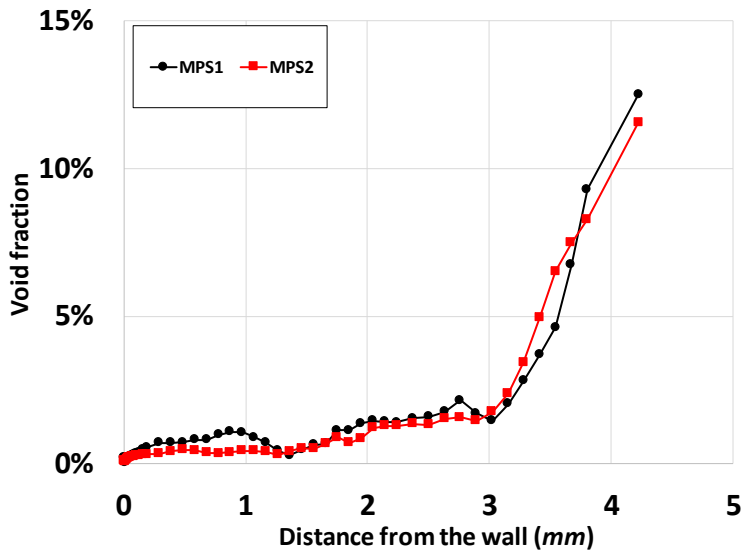

Fig. 11. Void fraction profiles at locations MPS1 and MPS2.

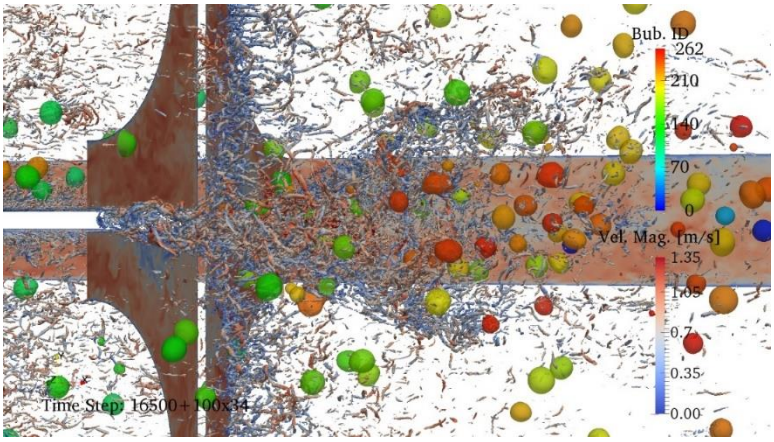

Fig. 12. A zoom-in view about the bubbles in the wake flows of spacer grid and mixing vanes (the bubble color indicates its ID used in bubble tracking algorithms).

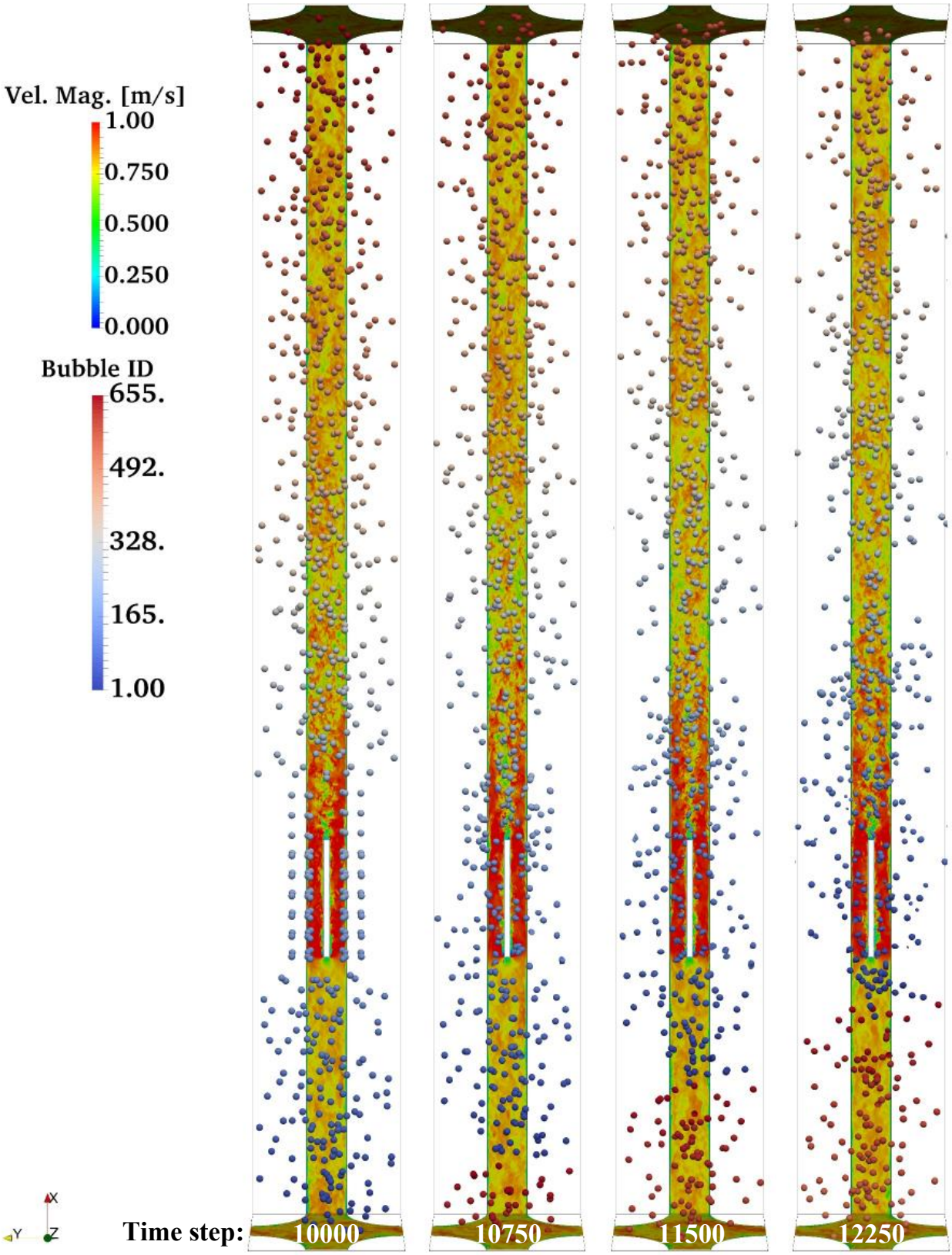

Fig. 13. The simulated bubbles rising in the vertical long subchannel (LSC) with the instantaneous velocity shown on the back, top and bottom slices.

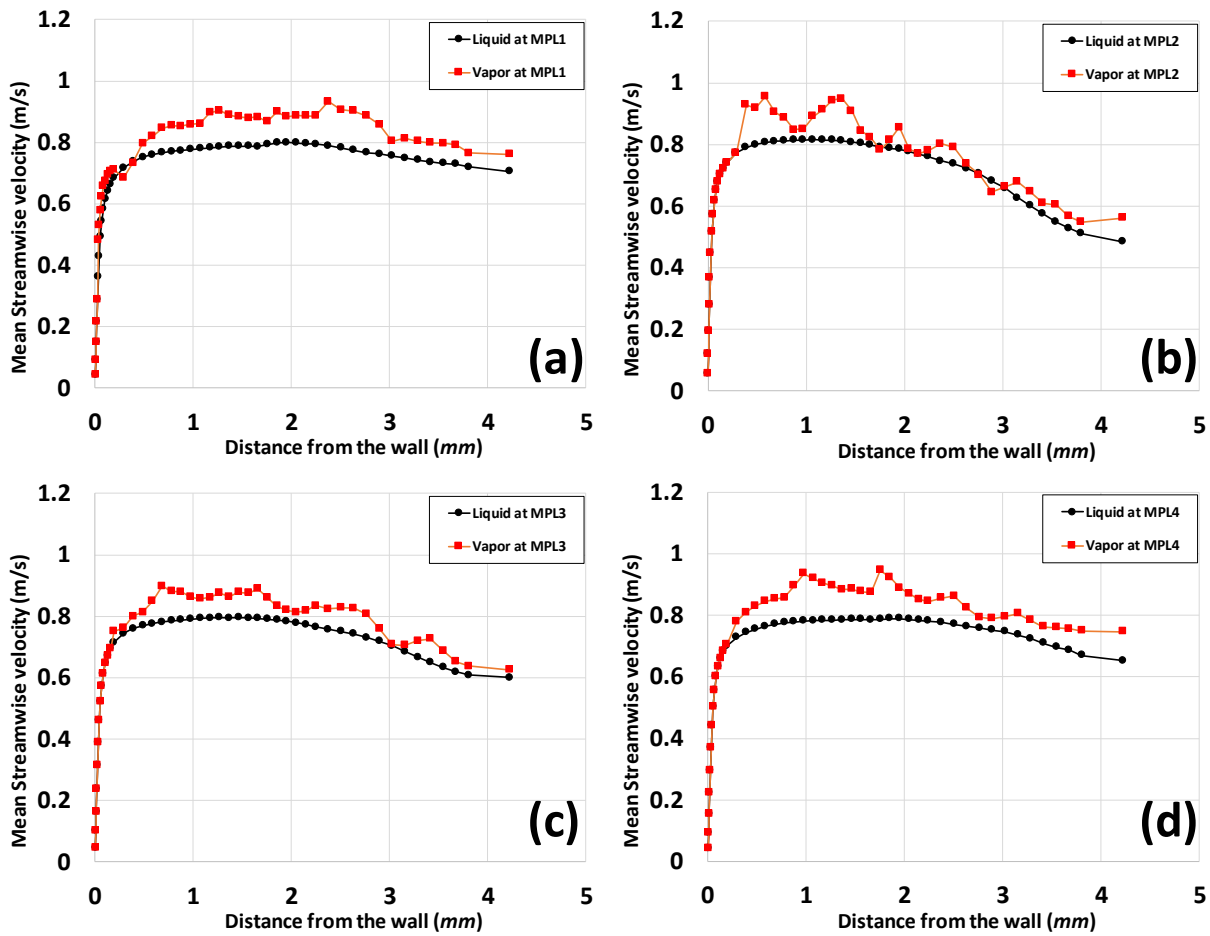

Fig. 14. Distributions of mean liquid and vapor streamwise velocity at four separate measurement locations in the long subchannel LSC.

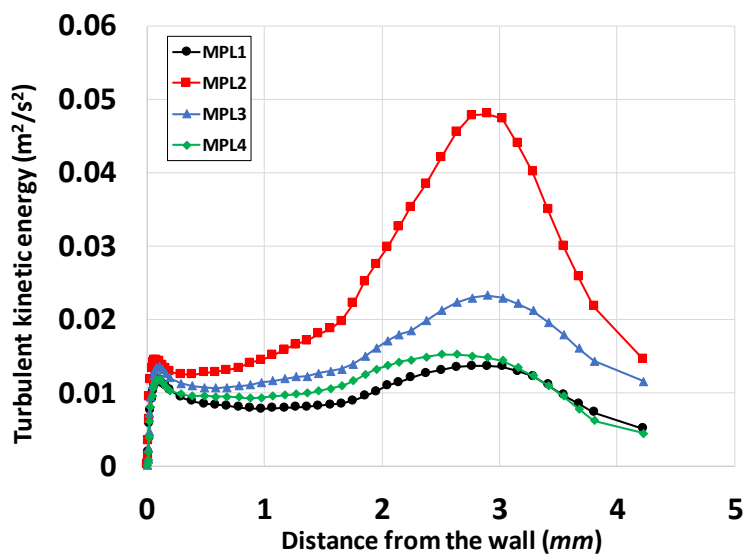

Fig. 15. Turbulent kinetic energy profiles at four separate measurement locations in the long subchannel LSC.

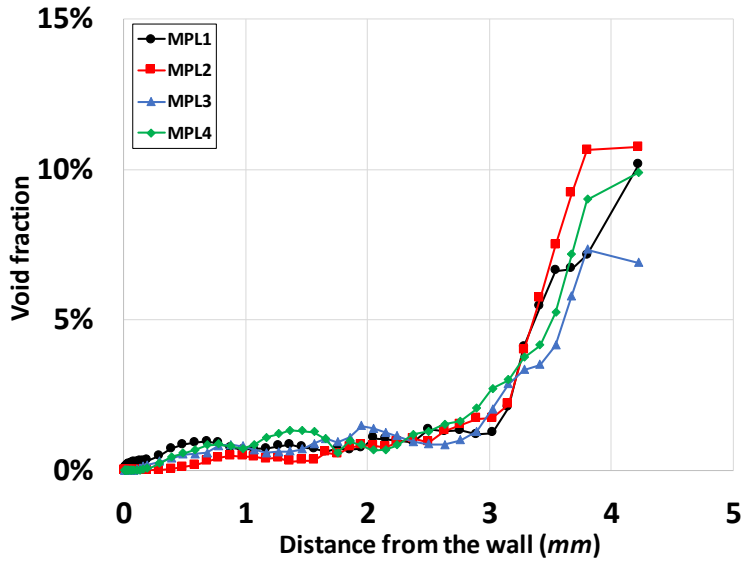

Fig. 16. Void fraction profiles at four separate measurement locations in the long subchannel LSC.

As previously mentioned, the bubble tracking method can record detailed bubble information for each individual bubble within the flow over the course of the bubbly flow simulation. Processing this numerical data can provide new ways to visualize and understand the bubble behavior. While the specific effects of the mixing vane and spacer grid subchannel geometries are difficult to observe in the void fraction profiles, bubble tracking analysis can offer new insights into their effects. As seen in Fig. 17, the intense swirling effect of the mixing vanes upon the bubbles is easily observed, giving a greater perspective on the evolution of the bubble locations within the subchannel.

A more detailed analysis of the bubble behavior can be achieved by dividing the bubbles into separate groups based on their distance to the wall (Table III), or their distance from the inlet patch of the domain (Table IV). For this analysis, the numerical data collected from the bubble tracking method was split into seven bubble groups based on their distance to the fuel rod wall and eight groups based on their distance to the domain inlet. The position of bubble's center of gravity is used as the bubble position. The group boundaries for each of these splitting techniques are listed in Table III and Table IV. For the distance to wall groups, the initial outer group bound was set at a distance of 1.5 bubble radii from the wall of the subchannel, and the sequential groups increase in width by a factor of 1.1. While the initial bubble size

limits the amount of data that can be gathered from the viscous sublayer in the near wall region, bubble behavior and dynamics can still be assessed within the turbulent log-law region. Additionally, for each grouping type, numerical data collected from within the mixing vane and spacer grid region was suppressed due to the complicated relation of the distance to the wall and the mixing vane geometry. Performing the splitting into the different groups allows to observe the migration of the bubbles within the subchannel. Two-phase flow simulations typically have a void fraction that peaks closer to the wall and previous subchannel simulations that excluded the mixing vane and spacer grid geometry observed a trend of the bubbles to migrate towards the wall[13]. For the LSC domain, the turbulent mixing generated by the mixing vanes results in a more balanced distribution of the bubbles throughout the channel as seen in Fig. 18.

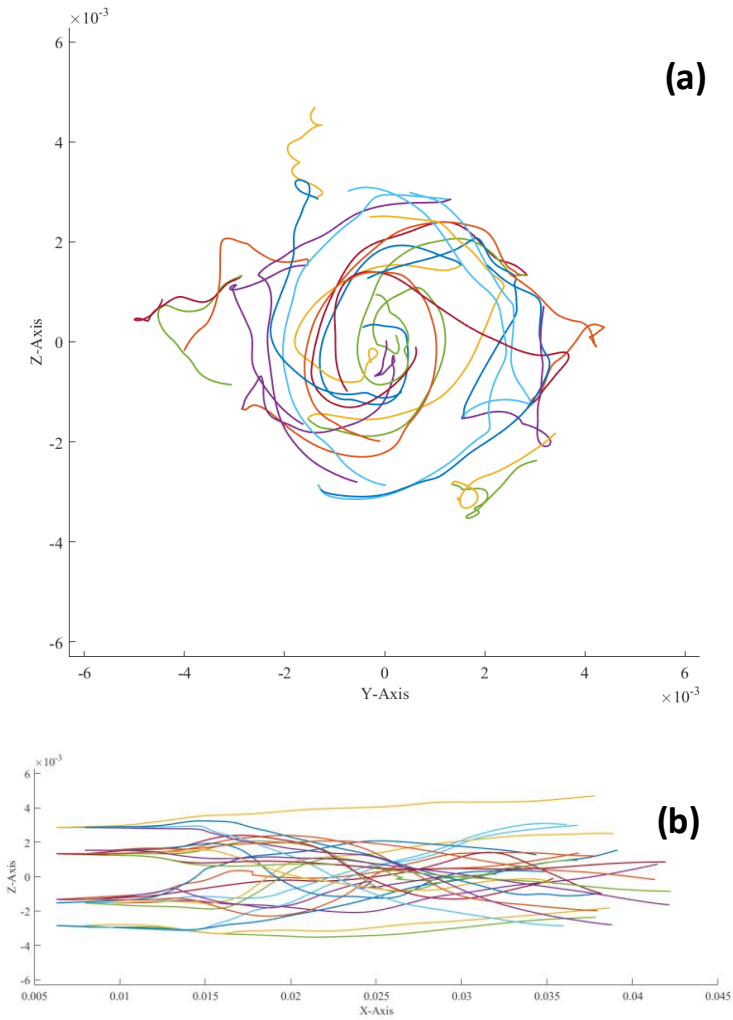

Fig. 17. Bubble trajectories in the subchannel SSC viewed from the inflow direction (a) and front side (b).

Table III: Group defined based on the distance to the wall.

Group Number	**Spatial Range of Each Group (by wall distance, unit: *mm*)**	**Range in y^+ Value**
W1	(0, 0.49]	(0, 147.34]
W2	(0.49, 1.03]	(147.34, 309.41]
W3	(1.03, 1.62]	(309.41, 487.69]
W4	(1.62, 2.27]	(487.69, 683.79]
W5	(2.27, 2.98]	(683.79, 899.51]
W6	(2.98, 3.77]	(899.51, 1136.80]
W7	(3.77, 4.34]	(1136.80, 1309.67]

Table IV: Groups defined based on the distance from the inlet patch.

Group Number	**Spatial Range of Each Group (by x coordinate, unit: *mm*)**
I1	(-20.0, -10.0]
I2	(-10.0, 0.0]
I3	(20.0, 30.0]
I4	(30.0, 40.0]
I5	(40.0, 50.0]
I6	(50.0, 60.0]
I7	(60.0, 70.0]
I8	(70.0, 80.0)

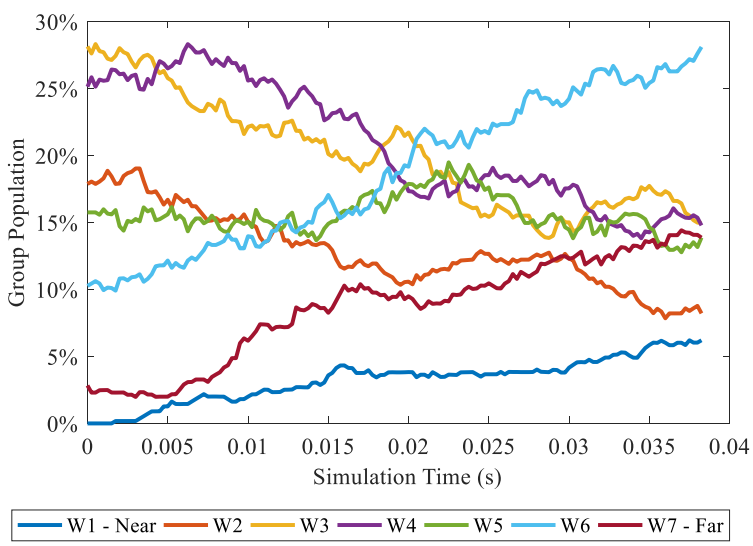

Fig. 18. Bubble population history in each distance to wall group for subchannel LSC.

For the calculation of additional bubble statistics, such as the drag coefficient, the solution is assumed to have reached a quasi-steady state condition when the relative bubble/liquid velocity stabilizes in the streamwise direction as seen in Fig. 19. Once this stabilized regime is achieved, a force balance between the bubble drag and buoyancy forces is assumed, allowing for the calculation of the drag coefficient for

each bubble. Averaging this data, the drag coefficient can be calculated for each distance to the wall group to create a relation between it and the distance to the wall as presented in Fig. 20. Overall, an increase of the drag coefficient is seen with an increased distance to the wall, hinting that the constant drag coefficient applied to lower resolution multiphase CFD simulations may not be sufficient to fully represent the bubble behavior.

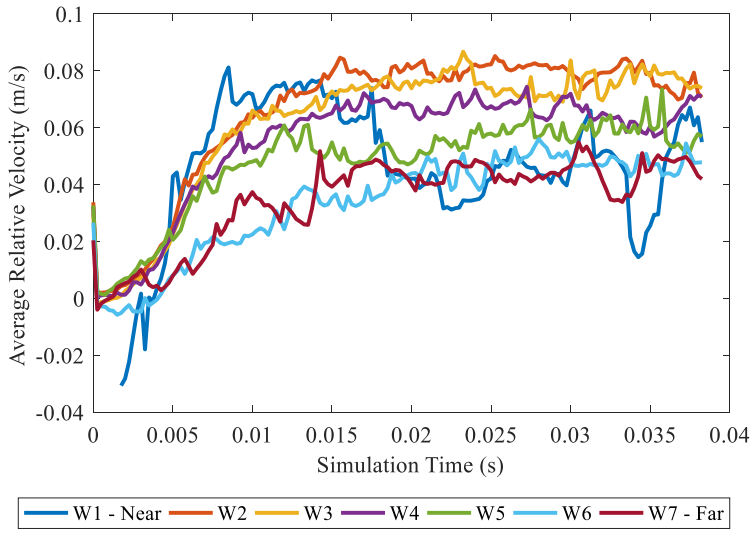

Fig. 19. Average bubble relative velocity for the distance to the wall group.

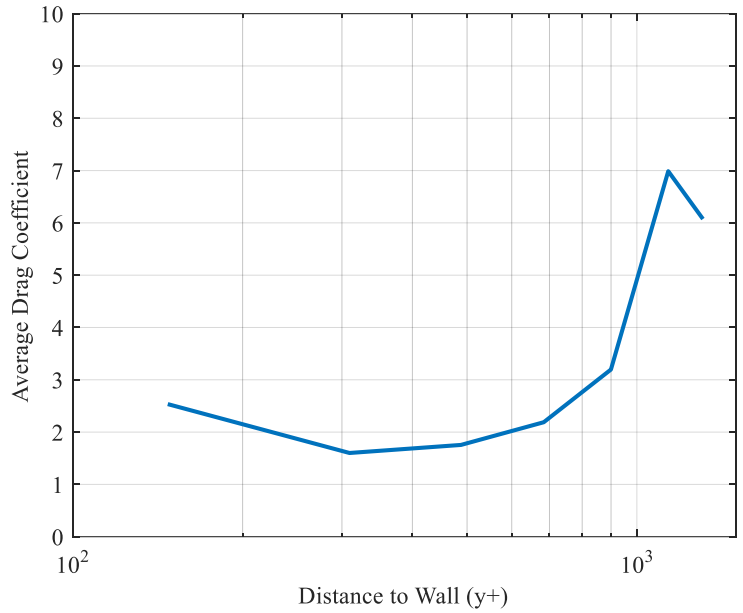

Fig. 20. Average group drag coefficient based on the distance to the wall.

Further processing of the bubble tracking numerical data can be completed to observe the trends of the bubble behavior over the length of the domain. Each distance to the wall group can be split into groups based on the distance the bubble is from the inlet of the domain in the streamwise direction. This analysis displays the evolution of bubble dynamics as they are affected by the spacer grid and mixing vane (SGMV) geometry. Fig. 21 and Fig. 22 display the impact that the subchannel geometry has upon the bubble/liquid relative velocity and the calculated average drag coefficient respectively. Each vertical stack represents the analysis results at a specific location away from the inlet. The markers within the stack indicate the group averaged quantity with respect to the wall distance from rod surface. An averaging of all wall distance groups at separate streamwise locations is also illustrated with the black circles. The red lines in these figures depict the start and end of SGMV region within the LSC domain. After exiting this region, the bubbles have a noted lower relative velocity, coupled with a higher calculated drag coefficient. The reduction in bubble relative velocity indicates a strong 'mixing' effect the SGMV have on the bubbly flow. Traveling through the remainder of the domain, each of these quantities returns to approximately the same value that was observed before the spacer grid and mixing vane region was entered. A closer analysis on the distribution of bubble drag coefficient before and after the SGMV are shown in Fig. 23 and Fig. 24. A significant number of bubbles is experiencing a high drag coefficient (the rightmost bin) at both locations. A Poisson distribution is otherwise observed for the drag coefficient spanning from 0 to 9.5. Because of the SGMV, a clear shift is observed about the bubble population from small drag coefficient bins to the large drag coefficient bin. This is a direct result of the relative velocity reduction caused by SGMV, and the different phases tend to have more 'homogenous' velocities when exiting the SGMV region.

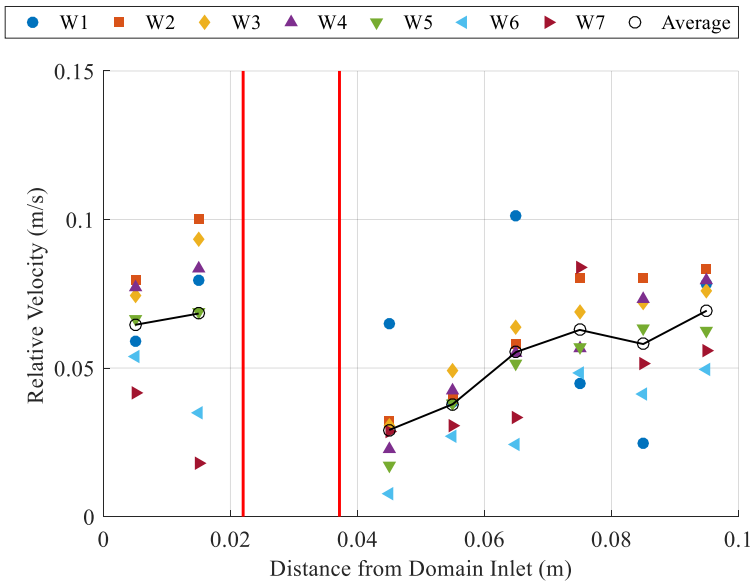

Fig. 21. Evolution of the average relative velocity for each distance to the wall group as a function of the distance from the domain inlet.

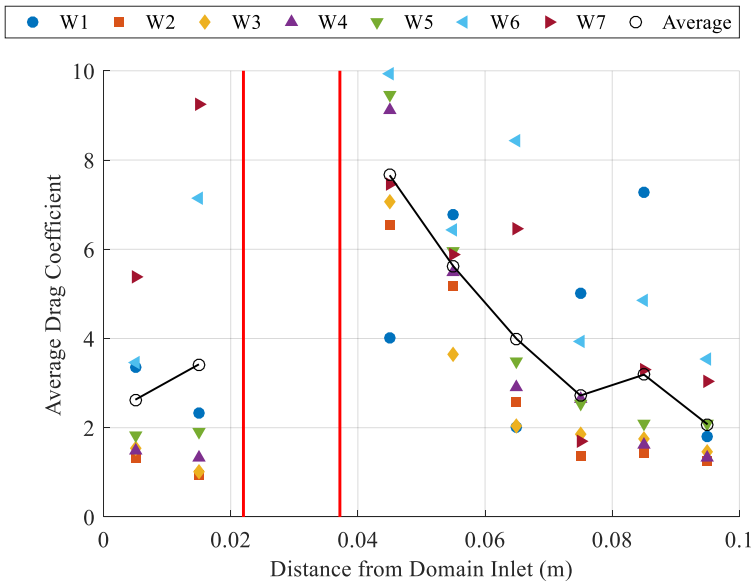

Fig. 22. Evolution of the average drag coefficient for each distance to the wall group throughout the LSC domain.

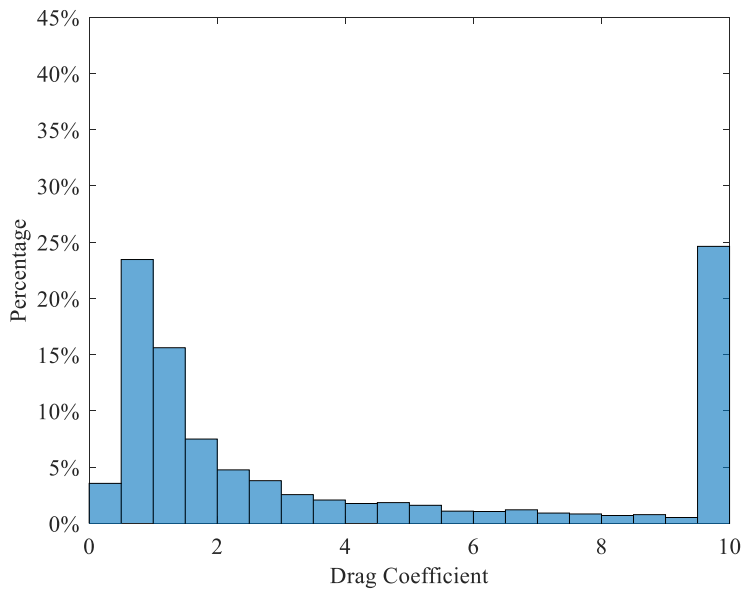

Fig. 23. Distribution of bubble drag coefficient immediately before bubbles enter the spacer grid and mixng vane region.

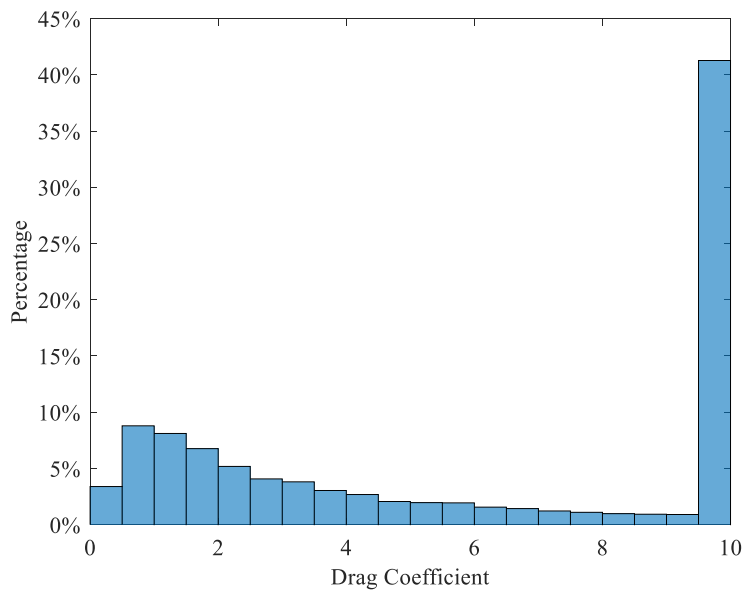

Fig. 24. Distribution of bubble drag coefficient immediately after bubbles exit the spacer grid and mixing vane region.

The bubble tracking method also allows for the collection of unique bubble statistics which offer novel insights into bubble behavior. These statistics, such as the deformability of the bubble[22], could be used to improve the calculation of lift coefficients implemented in lower resolution multiphase CFD. The bubble deformability factor (γ_d) is defined as the ratio of the minimum value of the level set distance field inside a bubble to the equivalent radius of a sphere which has the same volume as the considered bubble. This

term quantifies how deformed a bubble is, with a perfect sphere having a value of $\gamma_d = 1.0$. The effect of the spacer grid and mixing vane geometry can again be observed in Fig. 25, where the bubbles leaving this region are notably more deformed than those entering.

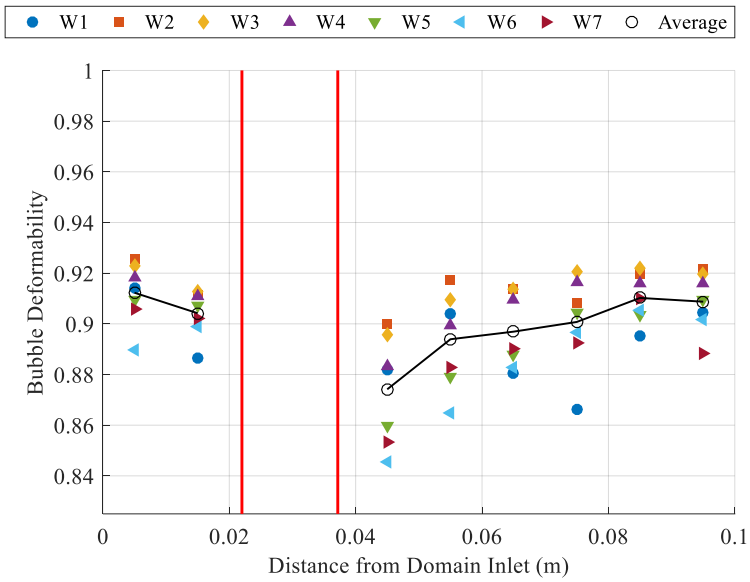

Fig. 25. Bubble deformability evolution for each distance to the wall group over the LSC domain.

V. CONCLUSIONS

In the presented research, the bubbly flows in PWR subchannel geometries are studied with high-fidelity interface tracking simulations due to its important role in reactor thermal-hydraulics analyses. The liquid turbulence is resolved by DNS while the interface behavior is captured by the level set method. Two subchannel geometries with different heights are considered. Both the time averaging analysis and advanced bubble tracking analysis are performed to process the simulation results. The geometric effects of subchannel structures on bubble behavior are discussed. The presence of spacer grid and mixing vanes substantially changes the bubbly flow characteristics in the subchannel. The centrifugal effect is identified in the wake flows downstream mixing vanes. The center peaked void fraction profile is observed. The location of TKE peak displays a dependency on the size and orientation of the mixing vanes. The influence of the spacer grid and mixing vanes generally decays as the downstream flow move further away from the mixing vanes.

By coupling two-phase flow simulations of PWR subchannels with the novel bubble tracking method, further insights into the dynamics of bubbly flows can be achieved. Bubbles can be split into multiple groups based on their distance to the wall for further statistical analysis. The numerical data processed displays an significant dependency of some bubble statistics on the distance to the wall, such as the drag coefficient or the bubble deformability. These dependencies suggest that more advanced calculations of the drag coefficient may be required for use in lower resolution multiphase CFD models. Numerical data gathered by the bubble tracking algorithm has also promoted even more novel ways of viewing statistical bubble data, such as the dynamic bubble trajectories. As simulations become more accurate in modeling the behavior of bubble dynamics within PWR geometries, these advanced statistical analysis tools will help shed light onto the bubbly flows inside PWR relevant geometries and better assess the influence of spacer grid and mixing vanes on two-phase coolant flows.

ACKNOWLEDGMENTS

The authors would like to acknowledge the support from the Consortium for Advanced Simulation of Light Water Reactors (CASL) (http://www.casl.gov) and the Aurora Early Science Program (ESP) at Argonne National Laboratory. CASL is an Energy Innovation Hub for Modeling and Simulation of Nuclear Reactors under U.S. Department of Energy (DOE) [grant number DE-AC05-00OR22725]. Argonne is operated by UChicago Argonne, LLC, for the U.S. DOE under contract DE-AC02-06CH11357. This research utilized computational resources provided by Argonne Leadership Computing Facility (ALCF), which is a DOE Office of Science User Facility supported under Contract DE-AC02-06CH11357. The solutions presented made use of software components provided by Altair Engineering, Simmetrix (MeshSim and SimModeler), SCOREC at RPI (Chef) and Kitware (ParaView).

REFERENCES

1. T. KUNUGI, “Brief review of latest direct numerical simulation on pool and film boiling,” Nucl. Eng. Technol. **44** 8, 847 (2012); https://doi.org/10.5516/NET.02.2012.717.

2. L. S. TONG, “An evaluation of the departure from nucleate boiling in bundles of reactor fuel rods,” Nucl. Sci. Eng. **33** 1, 7 (1968); https://doi.org/10.13182/NSE68-A20912.

3. E. MERZARI, H. NINOKATA, and E. BAGLIETTO, “Numerical simulation of flows in tight-lattice fuel bundles,” Nucl. Eng. Des. **238** 7, 1703, North-Holland (2008); https://doi.org/10.1016/J.NUCENGDES.2008.01.001.

4. P. J. TURINSKY and D. B. KOTHE, “Modeling and simulation challenges pursued by the Consortium for Advanced Simulation of Light Water Reactors (CASL),” J. Comput. Phys. **313**, 367 (2016); https://doi.org/10.1016/j.jcp.2016.02.043.

5. C. RABITI, A. ALFONSI, and A. EPINEY, “New Simulation Schemes and Capabilities for the PHISICS/RELAP5-3D Coupled Suite,” Nucl. Sci. Eng. **182** 1, 104, Taylor & Francis (2016); https://doi.org/10.13182/NSE14-143.

6. R. C. WANG et al., “Validation of the U.S. NRC Coupled Code System TRITON/TRACE/PARCS Using the Special Power Excursion Reactor Test III,” Nucl. Technol. **183** 3, 504, Taylor & Francis (2013); https://doi.org/10.13182/NT13-A19437.

7. J. G. KIRKWOOD, “Statistical mechanics of fluid mixtures,” J. Chem. Phys. **3** 5, 300 (1935); https://doi.org/10.1063/1.1749657.

8. T. Von KARMAN, “The fundamentals of the statistical theory of turbulence,” J. Aeronaut. Sci. **4** 4, 131 (1937); https://doi.org/10.2514/8.350.

9. D. CHISHOLM, “A theoretical basis for the Lockhart-Martinelli correlation for two-phase flow,” Int. J. Heat Mass Transf. **10** 12, 1767 (1967); https://doi.org/10.1016/0017-9310(67)90047-6.

10. M. ISHII, *Thermo-fluid dynamic theory of two-phase flow*, Paris (1975).

11. R. T. LAHEY and D. A. DREW, “On the development of multidimensional two-fluid models for vapor/liquid two-phase flows,” Chem. Eng. Commun. **118** 1, 125, Taylor & Francis (1992); https://doi.org/10.1080/00986449208936090.

12. A. PROSPERETTI and G. TRYGGVASON, *Computational methods for multiphase flow*, Cambridge university press (2007).

13. J. FANG et al., “Direct numerical simulation of reactor two-phase flows enabled by high-performance computing,” Nucl. Eng. Des. **330**, 409 (2018); https://doi.org/10.1016/j.nucengdes.2018.02.024.

14. G. TRYGGVASON et al., “Direct Numerical Simulations of Multiphase Flows,” in Direct and Large-Eddy Simulation IV, B. J. Geurts, R. Friedrich, and O. Métais, Eds., pp. 517–526, Springer Netherlands, Dordrecht (2001); https://doi.org/10.1007/978-94-017-1263-7_60.

15. G. TRYGGVASON, A. ESMAEELI, and N. AL-RAWAHI, “Direct numerical simulations of flows with phase change,” Comput. Struct. (2005); https://doi.org/10.1016/j.compstruc.2004.05.021.

16. C. W. HIRT and B. D. NICHOLS, “Volume of fluid (VOF) method for the dynamics of free boundaries,” J. Comput. Phys. **39** 1, 201 (1981); https://doi.org/10.1016/0021-9991(81)90145-5.

17. S. O. UNVERDI and G. TRYGGVASON, “A front-tracking method for viscous, incompressible, multi-fluid flows,” J. Comput. Phys. **100** 1, 25 (1992); https://doi.org/10.1016/0021-9991(92)90307-K.

18. M. SUSSMAN, P. SMEREKA, and S. OSHER, “A level set approach for computing solutions to incompressible two-phase flow,” J. Comput. Phys. **114** 1, 146 (1994); https://doi.org/10.1006/jcph.1994.1155.

19. J. MA, C.-T. HSIAO, and G. L. CHAHINE, “A Physics Based Multiscale Modeling of Cavitating Flows,” Comput. Fluids **145**, 68, Pergamon (2016); https://doi.org/10.1016/J.COMPFLUID.2016.12.010.

20. J. FANG and I. A. BOLOTNOV, “Development of Bubble Tracking Capability for Level-Set Interface Tracking Method,” in 2014 ANS Winter Meeting **111**, pp. 1658–1659, American Nuclear Society (2014).

21. J. FANG and I. A. BOLOTNOV, “Application of Bubble Tracking Capability for Turbulent Two-phase Flow Simulations of a PWR Subchannel,” in 2015 ANS winter meeting **113**, pp. 1549–1551, American Nuclear Society (2015).

22. J. FANG and I. A. BOLOTNOV, “Bubble tracking analysis of PWR two-phase flow simulations

based on the level set method," Nucl. Eng. Des. **323** Supplement C, 68 (2017); https://doi.org/10.1016/j.nucengdes.2017.07.034.

23. S. NAGRATH, K. E. JANSEN, and R. T. LAHEY, "Computation of incompressible bubble dynamics with a stabilized finite element level set method," Comput. Methods Appl. Mech. Eng. **194** 42, 4565 (2005); https://doi.org/10.1016/j.cma.2004.11.012.

24. I. A. BOLOTNOV et al., "Detached direct numerical simulations of turbulent two-phase bubbly channel flow," Int. J. Multiph. Flow **37** 6, 647, Pergamon (2011); https://doi.org/10.1016/j.ijmultiphaseflow.2011.03.002.

25. H. YI et al., "In-situ visualization and computational steering for large-scale simulation of turbulent flows in complex geometries," in Proceedings of 2014 IEEE International Conference on Big Data (Big Data), pp. 567–572 (2014); https://doi.org/10.1109/BigData.2014.7004275.

26. M. RASQUIN et al., "Scalable implicit flow solver for realistic wing simulations with flow control," Comput. Sci. Eng. **16** 6, 13 (2014); https://doi.org/10.1109/MCSE.2014.75.

27. C. H. WHITING and K. E. JANSEN, "A stabilized finite element method for the incompressible Navier-Stokes equations using a hierarchical basis," Int. J. Numer. Methods Fluids **35** 1, 93 (2001); https://doi.org/10.1002/1097-0363(20010115)35:1<93::AID-FLD85>3.0.CO;2-G.

28. J. U. BRACKBILL, D. B. KOTHE, and C. ZEMACH, "A continuum method for modeling surface tension," J. Comput. Phys. **100** 2, 335 (1992); https://doi.org/10.1016/0021-9991(92)90240-Y.

29. S. OSHER and J. A. SETHIAN, "Fronts propagating with curvature-dependent speed: algorithms based on Hamilton-Jacobi formulations," J. Comput. Phys. **79** 1, 12 (1988); https://doi.org/10.1016/0021-9991(88)90002-2.

30. A. M. THOMAS et al., "Estimation of shear-induced lift force in laminar and turbulent flows," Nucl. Technol. **190** 3, 274 (2015); https://doi.org/10.13182/NT14-72.

31. J. FANG, A. M. THOMAS, and I. A. BOLOTNOV, "Development of advanced analysis tools for interface tracking simulations," in ANS 2013 Winter Meeting **109**, pp. 1613–1615, American Nuclear Society (2013).

32. L. H. FICK, E. MERZARI, and Y. A. HASSAN, “Direct Numerical Simulation of Pebble Bed Flows: Database Development and Investigation of Low-Frequency Temporal Instabilities,” J. Fluids Eng. **139** 5, 51301 (2017).

33. I. A. BOLOTNOV, “Influence of Bubbles on the Turbulence Anisotropy,” J. Fluids Eng. **135** 5, 051301, ASME (2013); https://doi.org/10.1115/1.4023651.

34. U.S. NRC, “Westinghouse AP1000 Design Control Document Rev. 19” (2011).

35. J. FENG and I. A. BOLOTNOV, “Evaluation of Bubble-Induced Turbulence Using Direct Numerical Simulation,” Int. J. Multiph. Flow **93**, 92, Pergamon (2017); https://doi.org/10.1016/J.IJMULTIPHASEFLOW.2017.04.003.

36. C. W. SMITH et al., “Improving Unstructured Mesh Partitions for Multiple Criteria Using Mesh Adjacencies,” SIAM J. Sci. Comput. **40** 1, C47, Society for Industrial and Applied Mathematics (2018); https://doi.org/10.1137/15M1027814.

37. J. FANG, M. RASQUIN, and I. A. BOLOTNOV, “Interface tracking simulations of bubbly flows in PWR relevant geometries,” Nucl. Eng. Des. **312** Supplement C, 205 (2017); https://doi.org/10.1016/j.nucengdes.2016.07.002.